Supporting Information

Ce-Hydroxamate Metal-Organic Frameworks for Photocatalytic H$_2$ Generation

Xuan Feng [a], Wenying Li [b], Lei Yang [a], Ting Song [a], Zhaoming Xia [b], Qiuxue Lai [a], Xuemei Zhou [a]*, Hai Xiao [b]* and Chong Liu [a]*

[a] School of Chemical Engineering, Sichuan University, Chengdu 610065, China

[b] Department of Chemistry, Tsinghua University, Beijing 100084, China

Email: liuchong@scu.edu.cn (C.L.); haixiao@tsinghua.edu.cn (H.X.); xuemeizhou@scu.edu.cn (X.Z.).

Contents

1. General procedures

1.1 Materials and reagents

Dimethyl terephthalate (99%), hydroxylamine hydrochloride (≥99%), sodium hydroxide (≥96.0%), acetic acid (99.0%), Cerium (III) Nitrate Hexahydrate (99.0%), Chloroplatinic acid hydrate (37.5% Pt), Nafion (5 wt.% in mixture of lower aliphatic alcohols and water, contains 45% water), Na_2SO_4 (≥99.0%), EtOH (≥99.7%), Trimethylamine TMA (30% in water), N,N-Dimethylformamide (99.8%) were purchased from Adamas, and used as received. Ultrapure water was obtained from a Millipak® Express 40 system (Merk-Millipore, Darmstadt, Germany). All reagents and solvents were used without any previous purification unless specified.

1.2 Characterization

Optical images were acquired with a Rui Hong BM-500T optical microscope.

^{1}H NMR spectrum was collected on a JNM-ECZ400S/L1 (400 MHz) spectrometer (JEOL Ltd., Tokyo, Japan).

Powder X-ray diffraction (PXRD) patterns were collected using a Rigaku MiniFlex600 operating at 40 kV, 40 mA for Cu Kα, (λ = 1.54178 Å) with a scan speed of 10°/min from 3 to 50° at a step size of 0.01°.

Single-crystal XRD data were collected on a Bruker D8 Venture single crystal X-ray diffractometer (Mo Kα radiation, λ = 0.71073 Å). The data were collected and integrated to 0.85 Å and empirical absorption correction was applied. The structure was solved with direct method using SHELXT[1] and refined by full-matrix least-squares on F^2 using SHELXL[2] in Olex2.[3] All non-H atoms were located easily and refined anisotropically. Idealized atom positions were calculated for H atoms.

Thermogravimetric analysis (TGA) was carried out on a TA Discovery SDT 650 simultaneous thermal analyzer from room temperature to 800 °C at a heating rate of 10 °C/min in a N_2 flow of 100 mL/min.

UV-vis diffuse reflectance spectra were conducted on a Perkin-Elmer Lambda 750S using an integrating-sphere accessory. The measured wavelength range was 200–800 nm. $BaSO_4$ powder was used as a reference standard.

The photoluminescence (PL) spectra were recorded on an Edinburgh FLS1000 spectrophotometer with an excitation wavelength of 340 nm. The emission ranging 300–700 nm at room temperature was acquired. The samples were pressed into a pellet on quartz before measurement. The PL spectra for each sample was an average of three measurements. The fluorescence decay profiles were also recorded using the FLS1000 at the excitation wavelength of 340 nm.

Photoelectrochemical measurements were carried out on an Autolab PGSTAT204A electrochemical workstation, details are given in the experimental section of the main text. The quantity of H_2 generated was determined using GC9790II (Fuli Analytical Instruments Co, LTD.) gas chromatograph. The GC column was fitted with a thermal conductivity detector (TCD) and packed with 5A molecular sieves, argon was used as carrier gas at a flow rate of 40 mL/min. The temperature of sampler, oven and detector was room temperature, 60 ^{o}C and 120 ^{o}C, respectively.

Scanning electron microscopy (SEM) images were obtained using a ZEISS Sigma 300 with accelerating voltages of 0.02–30 kV.

2. Synthesis of ligand and MOFs

2.1 Synthesis of H$_2$-BDHA

The synthesis of ligand 1,4-benzenedihydroxamic acid (H$_2$-BDHA) was carried out according to the procedure previously reported.[4, 5] The identity and purity of the ligand were confirmed by ^{1}H NMR (Figure S1).
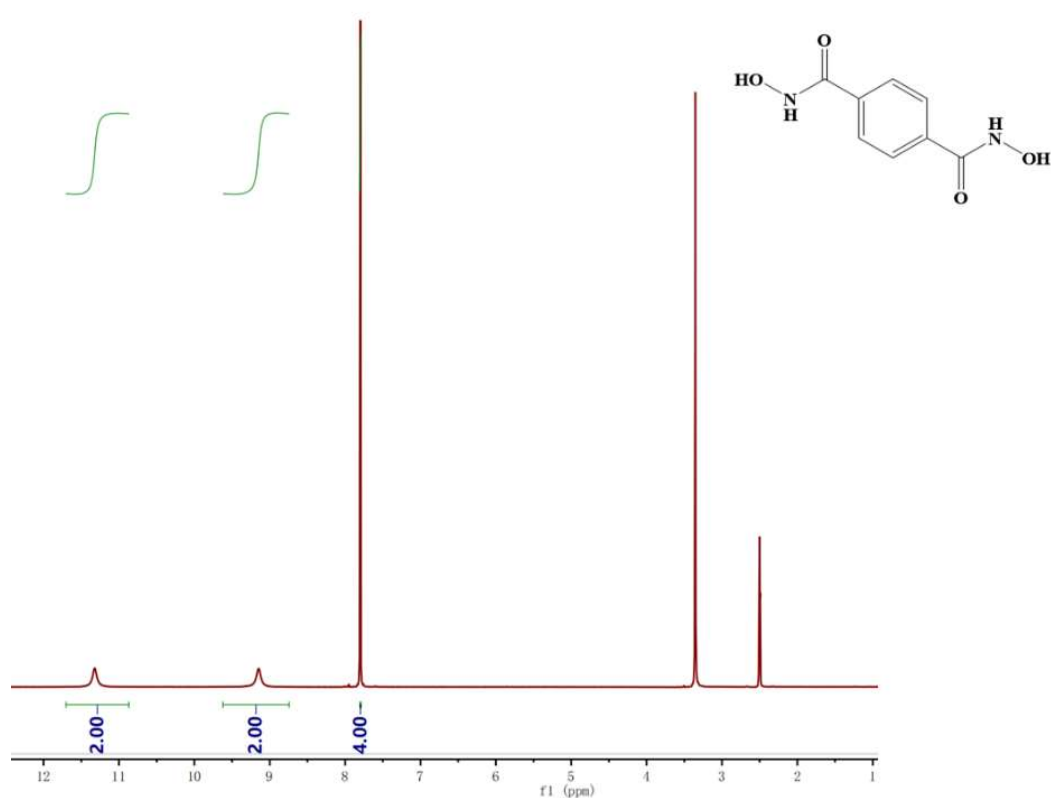

Figure S1. ^{1}H NMR spectrum of H$_2$-BDHA in DMSO-d_6.

2.2 Synthesis of SUM-6

H$_2$-BDHA (19.61 mg, 0.1 mmol) and Ce(NO$_3$)$_3$·6H$_2$O (217.11 mg, 0.5 mmol) were ultrasonically dissolved in 2.0 mL DMF in a 4 mL glass vial before being tightly sealed. The mixture was heated in an isothermal oven at 80 °C for 11 hours. Rod-shaped single crystals (Figure S2) were collected and washed with fresh DMF (3 × 1 mL), yield: 34.91% (calculated based on Ce). The crystal structure was determined via single crystal X-ray crystallography (CCDC depository number 2159905) and named SUM-6 (SUM = Sichuan University Materials).
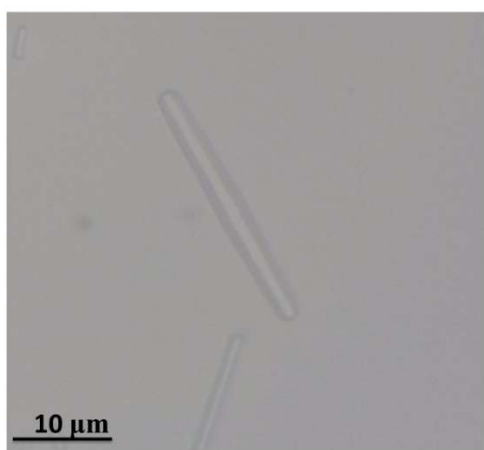

Figure S2. Optical image of SUM-6 crystals.

2.3 Synthesis of SUM-7

H$_2$-BDHA (11.76 mg, 0.06 mmol) and Ce(NO$_3$)$_3$·6H$_2$O (52.11 mg, 0.12 mmol) were ultrasonically dissolved in a mixture of DMF (2.0 mL) and acetic acid (0.8 mL) in a 4 mL glass vial before being tightly sealed. The mixture was heated in an isothermal oven at 100 ℃ for 16 hours. Rod-shaped single crystals (Figure S3) were collected and washed with fresh DMF (3 × 1 mL), yield: 19.70% (calculated based on Ce). The crystal structure was determined via single crystal X-ray crystallography (CCDC depository number 2159906) and named SUM-7.
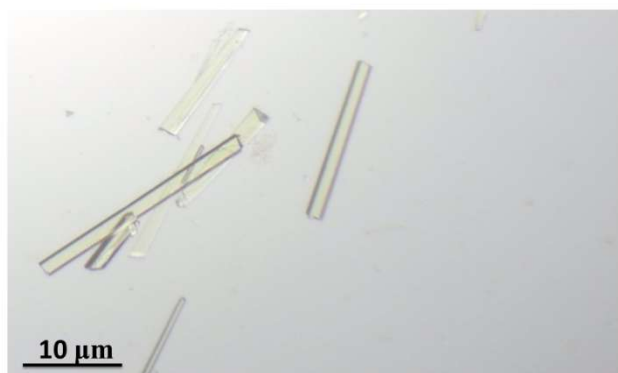

Figure S3. Optical image of SUM-7 crystals.

3. Characterization of MOFs

3.1 Crystallographic study of SUM-6 and SUM-7

Table S1. Crystal data and structure refinement details for SUM-6

CCDC depository number	2159905
Identification code	SUM-6
Empirical formula	$C_{14}H_{20}CeN_5O_9$
Formula weight	542.47
Temperature/K	304
Crystal system	monoclinic
Space group	C2/c
a/Å	13.9892(7)
b/Å	20.1086(9)
c/Å	8.5463(4)
$\alpha/°$	90
$\beta/°$	124.703(2)
$\gamma/°$	90
Volume/Å^3	1976.44(17)
Z	4
$\rho_{calc}g/cm^3$	1.823
μ/mm^{-1}	2.361
F(000)	1076
Crystal size/mm^3	$0.1 \times 0.07 \times 0.06$
Radiation	MoKα ($\lambda = 0.71073$)
2Θ range for data collection/°	4.052 to 54.99
Index ranges	$-18 \leq h \leq 18, -26 \leq k \leq 26, -10 \leq l \leq 11$
Reflections collected	15794
Independent reflections	2267 [$R_{int} = 0.0708$, $R_{sigma} = 0.0412$]
Data/restraints/parameters	2267/27/153
Goodness-of-fit on F^2	1.107
Final R indexes [I>=2σ (I)]	$R_1 = 0.0418$, $wR_2 = 0.1088$
Final R indexes [all data]	$R_1 = 0.0518$, $wR_2 = 0.1137$
Largest diff. peak/hole / e Å^{-3}	1.41/-1.01

Table S2. Crystal data and structure refinement details for SUM-7

CCDC depository number	2159906
Identification code	SUM-7
Empirical formula	$C_{10}H_9CeN_2O_6$
Formula weight	393.31
Temperature/K	304
Crystal system	tetragonal
Space group	$I4_122$
a/Å	17.450(3)
b/Å	17.450(3)
c/Å	16.295(4)
α/°	90
β/°	90
γ/°	90
Volume/Å^3	4961(2)
Z	8
ρ_{calc}g/cm^3	1.053
μ/mm^{-1}	1.847
F(000)	1512
Crystal size/mm^3	$0.43 \times 0.13 \times 0.09$
Radiation	MoKα (λ = 0.71073)
2Θ range for data collection/°	4.668 to 55.248
Index ranges	-22 ≤ h ≤ 22, -22 ≤ k ≤ 22, -21 ≤ l ≤ 21
Reflections collected	101387
Independent reflections	2891 [R_{int} = 0.1090, R_{sigma} = 0.0249]
Data/restraints/parameters	2891/27/94
Goodness-of-fit on F^2	1.045
Final R indexes [I>=2σ (I)]	R_1 = 0.0307, wR_2 = 0.0800
Final R indexes [all data]	R_1 = 0.0349, wR_2 = 0.0820
Largest diff. peak/hole / e Å^{-3}	1.07/-0.44
Flack parameter	0.50(2)
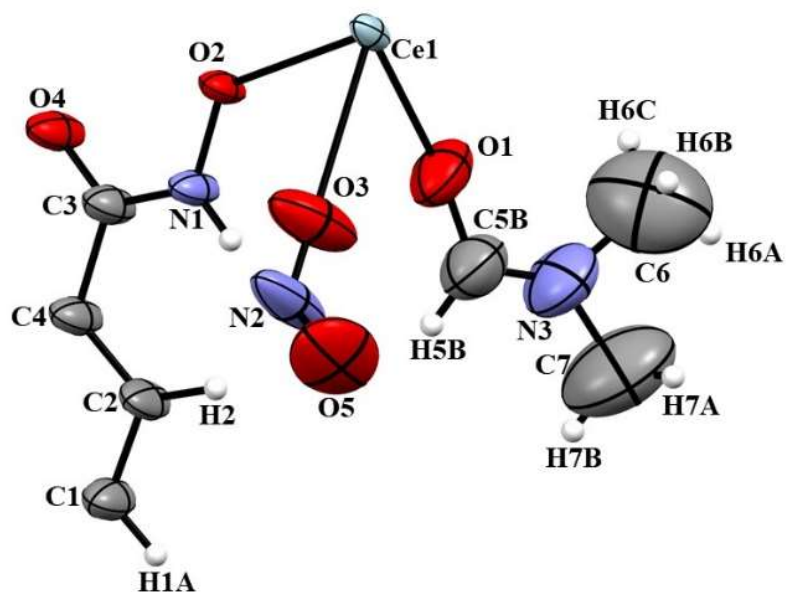
Figure S4. ORTEP diagram of the asymmetric unit of SUM-6 (50% probability factor for the thermal ellipsoids), generated via Mercury 3.6.[i]
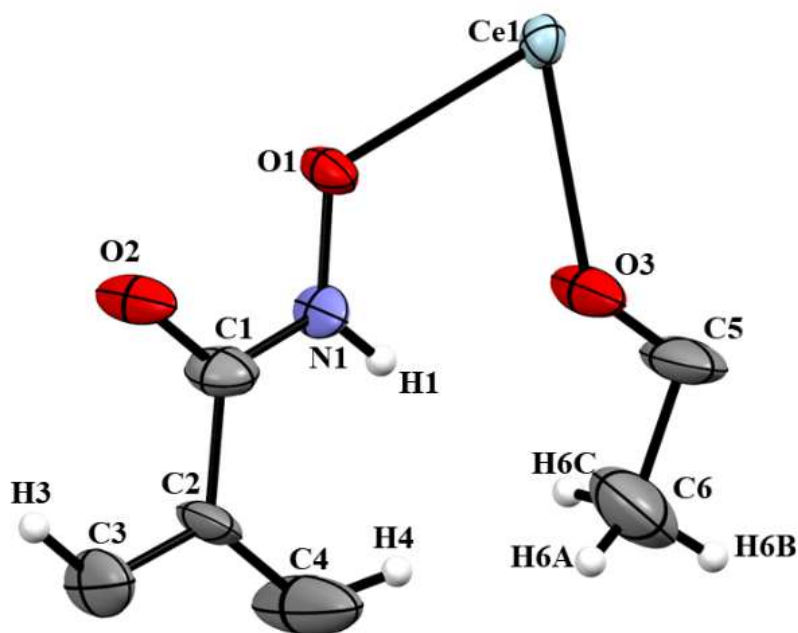

Figure S5. ORTEP diagram of the asymmetric unit of SUM-7 (50% probability factor for the thermal ellipsoids), generated via Mercury 3.6.[ii]

---

[i] Minor disordering that was observed for the nitrate anion and the DMF molecule was omitted here in the diagram for clarity.

[ii] The BDHA linker lies about a two-fold axis, therefore only half of the molecule is shown here in the asymmetric unit. The disordered acetate anion also lies on two-fold axis, in which the methyl carbon C6 is equally disordered over two adjacent sites.
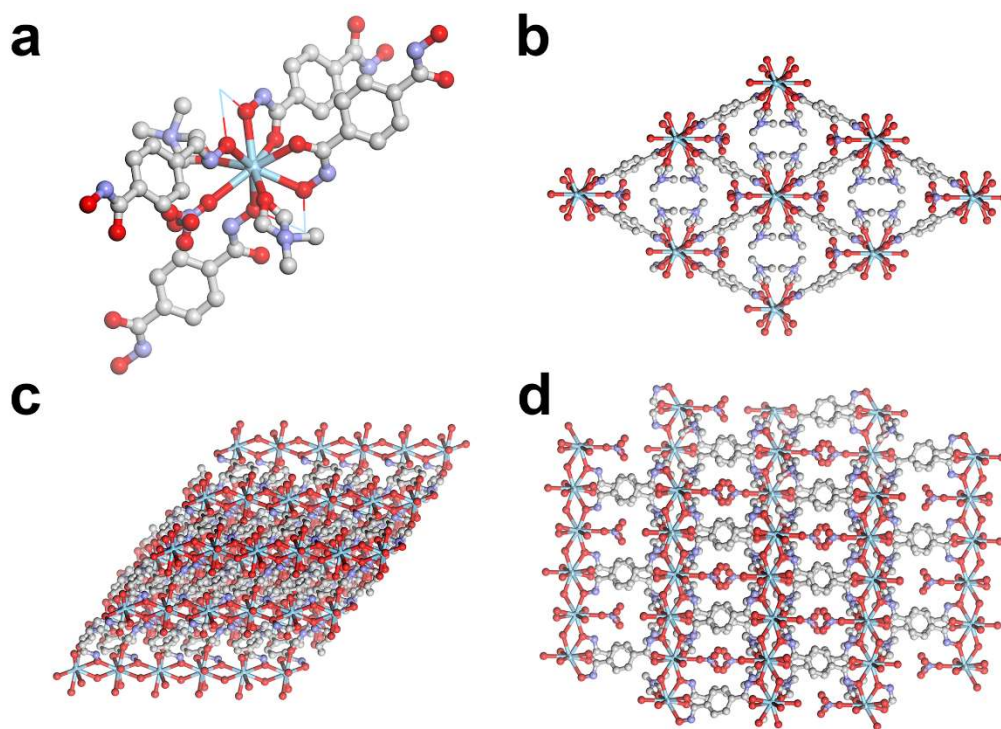
Figure S6. (a) Coordination environment of a Ce center in SUM-6; crystal structure of SUM-6 viewed in the z (b), y (c), and x (d) directions. Ce: blue spheres; C: light grey spheres; N: light blue spheres; O: red spheres; H: omitted for clarity.
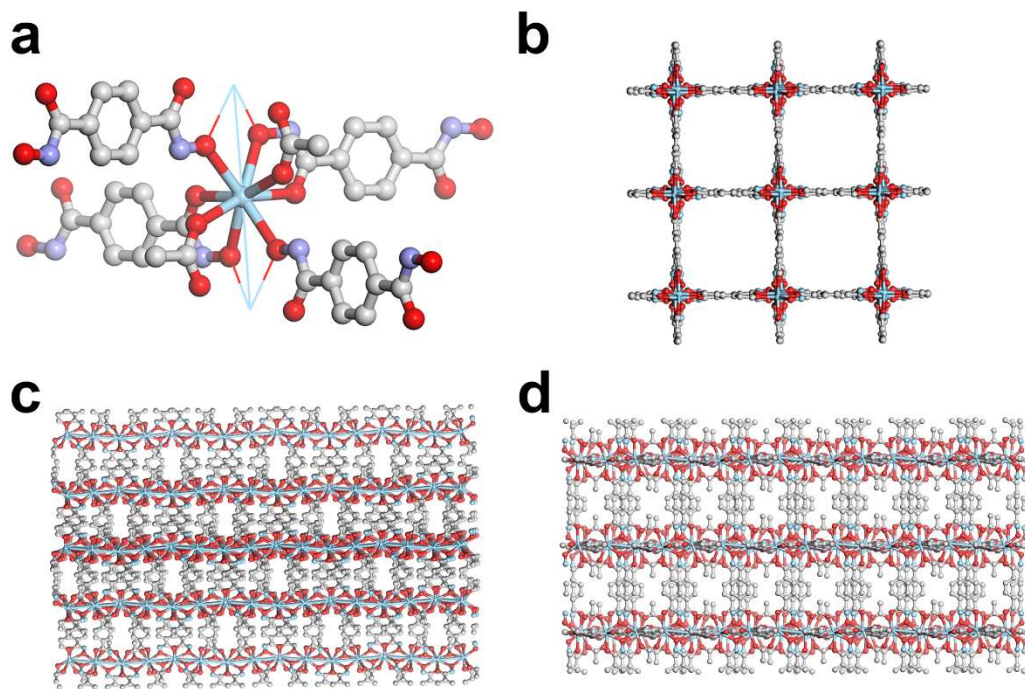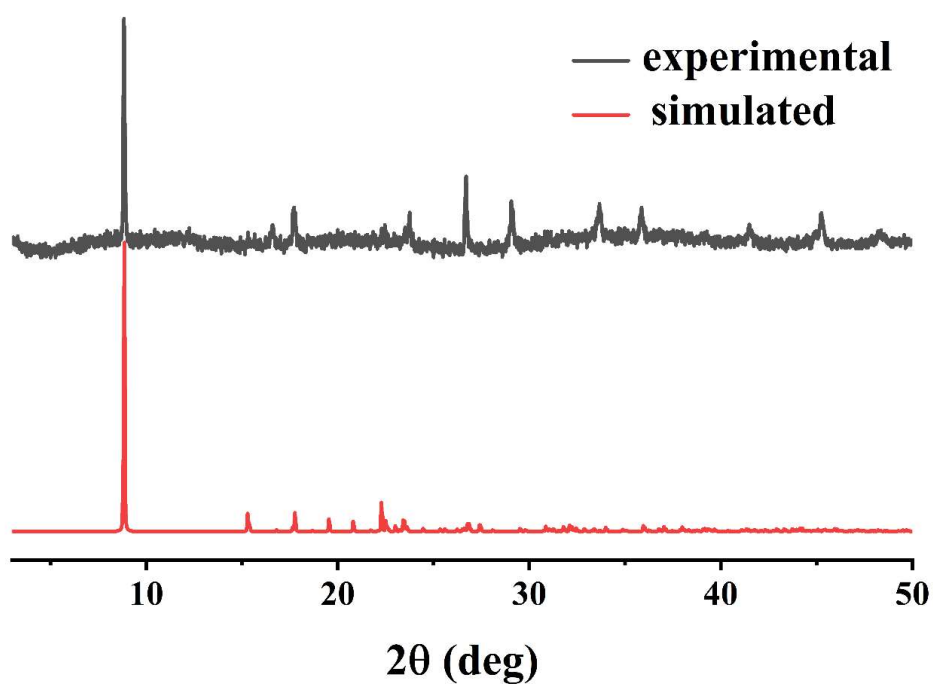
Figure S7. (a) Coordination environment of a Ce center in SUM-7; crystal structure of SUM-7 viewed in the z (b), y (c), and x (d) directions. Ce: blue spheres; C: light grey spheres; N: light blue spheres; O: red spheres; H: omitted for clarity.

Figure S8. PXRD patterns of SUM-6, comparing the experimental (black) and simulated (red) from SC-XRD data.
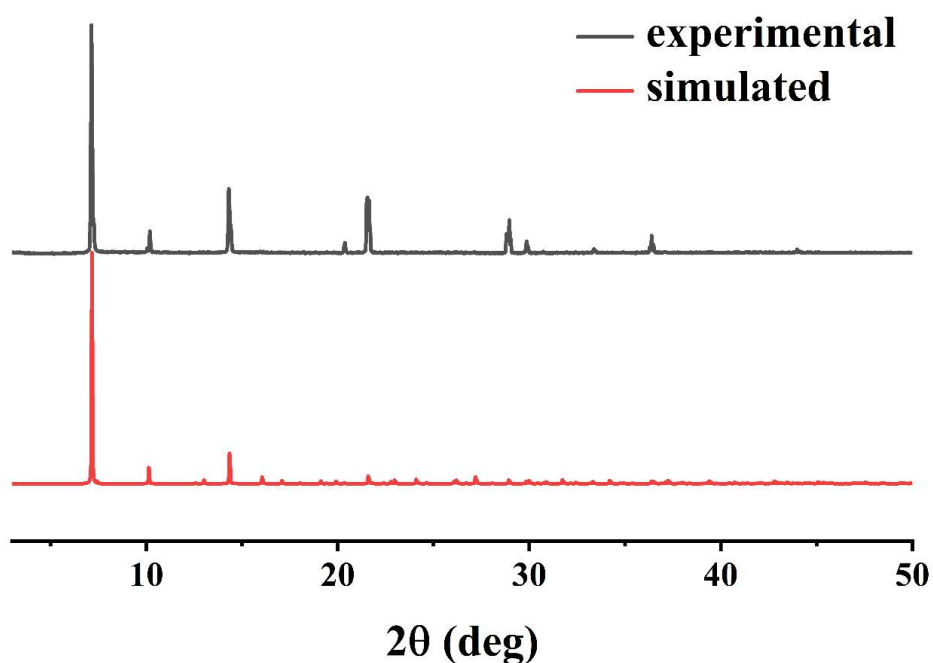
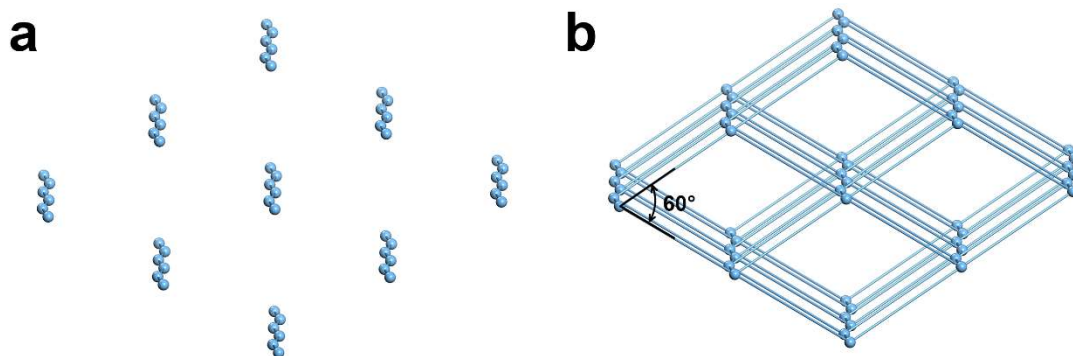**Figure S9.** PXRD patterns of SUM-7, comparing the experimental (black) and simulated (red) from SC-XRD data.

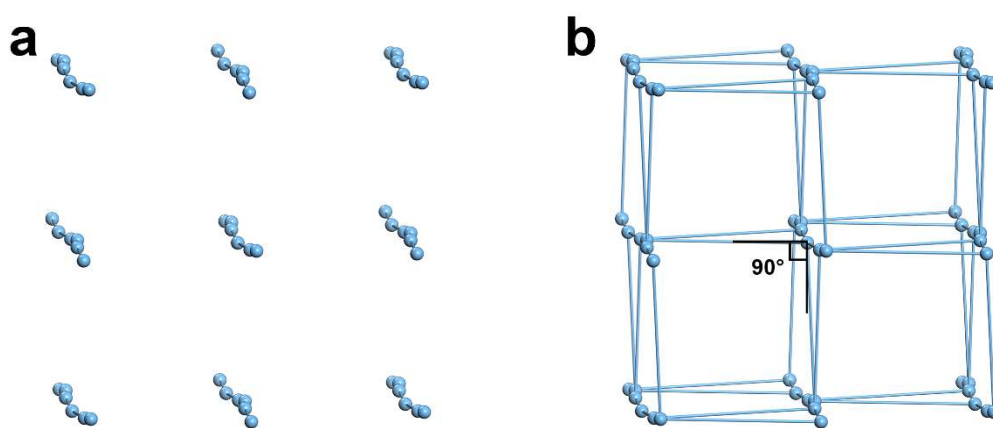**Figure S10.** Simplified schematic illustration of the 1D SBU (a) and connectivity (b) in SUM-6.

Figure S11. Simplified schematic illustration of the 1D SBU (a) and connectivity (b) in SUM-7.

3.2 Thermogravimetric analysis (TGA) and surface area calculation of SUM-6 and SUM-7

As shown in Figures S12 and S13, the initial stages of weight loss below 200 °C were observed for both SUM-6 and SUM-7, corresponding to the broad exothermic peaks (pointing up), were due to the removal of solvent molecules from the MOF pores. The second weight loss stages centered around 240 °C that were accompanied by relatively sharp exothermic peaks in the DTA plot, could be attributed to the early decomposition of the MOFs.
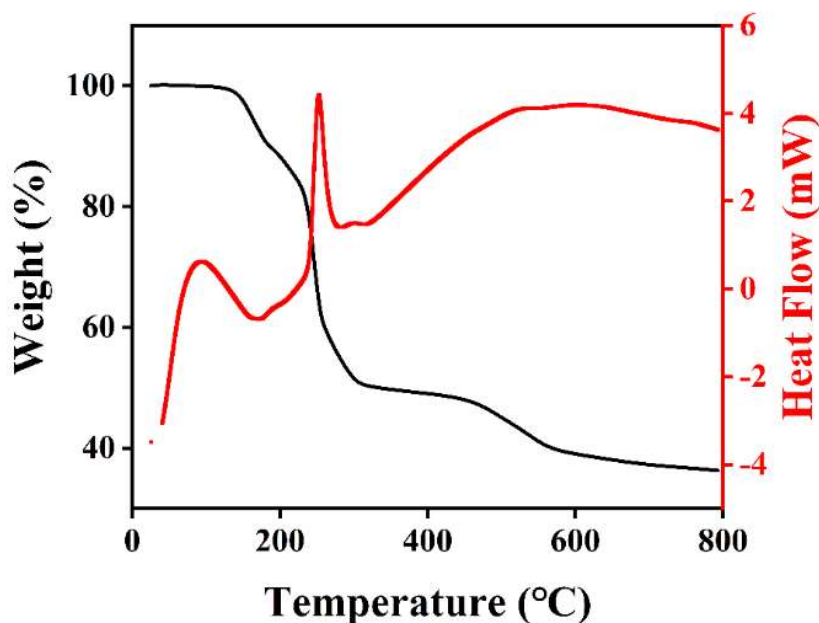

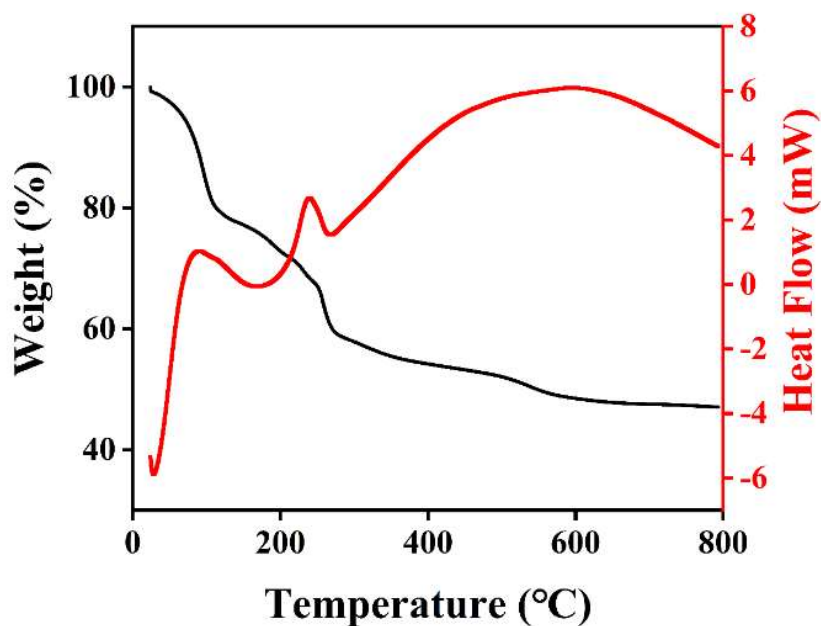**Figure S12.** TG and heat flow curves of SUM-6.

Figure S13. TG and heat flow curves of SUM-7.

Despite our best efforts trying to activate the MOFs for N_2 sorption using various organic solvents and supercritical CO_2, no appreciable N_2 uptake was observed. Therefore, the theoretical surface area of the MOFs was calculated using Materials Studio (Connolly radius = 1.8 Å), based on their respective SC-XRD structures. For SUM-6, the calculated surface area was 0 m^2/g; for SUM-7, the calculated surface area was 1377.40 m^2/g.

4. Electrochemical and photoelectrochemical characterization

4.1 UV-vis diffuse reflectance spectroscopy

UV-vis diffuse reflectance spectra (DRS) were collected on a Perkin-Elmer Lambda 750S using an integrating sphere. The measured wavelength range was 200–800 nm. $BaSO_4$ powder was used as a reference standard. The Tauc plot was derived from the DRS (Figure 2c in the main text) and shown below (Figure S14).
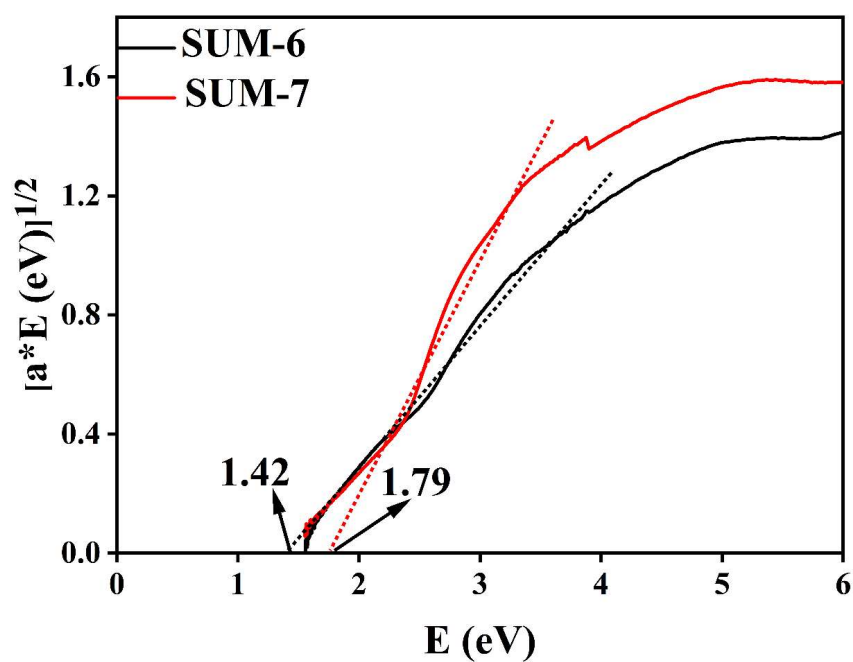

Figure S14. Tauc plots of SUM-6 (black) and SUM-7 (red).

Table S3. Summary of band gaps values in the literature

MOF	Band gap (eV)	H_2 generation rate ($\mu mol\ g^{-1}\ h^{-1}$)	Time (h)	Exp. or Calc.	Reference
Zr-UiO-67	3.02	26.78	3	Exp.	6
Ce-UiO-67	3.39	269.6	3	Exp.	6
Ce-UiO-66	2.82	n/a	n/a	Exp.	7
Ce-UiO-66-NO_2	2.79	n/a	n/a	Exp.	7
Ce-UiO-66-NH_2	2.09	n/a	n/a	Exp.	7
Ce-UiO-66-Br	2.68	n/a	n/a	Exp.	7
Ce-UiO-67	2.50	n/a	n/a	Exp.	7
Zr/Ce-UiO-66	3.25	4.5	24	Exp.	8
Zr/Ce/Ti-UiO-66	3.05	9.58	24	Exp.	8
Ce-UiO-66	2.60	3	24	Exp.	8
Ce-TTCA	2.08	15.8	4	Exp.	9
Ce-TTCA-33	2.00	32.9	4	Exp.	9
Ce-TTCA-46	1.90	58.6	4	Exp.	9
Ce-TTCA-65	1.78	95.8	4	Exp.	9
Ce-UiO-66	2.66	n/a	n/a	Calc.	10
Ce-UiO-66-NH_2	1.17	n/a	n/a	Calc.	10
Ce-UiO-66-NO_2	2.44	n/a	n/a	Calc.	10
Ce-UiO-66-F	2.45	n/a	n/a	Calc.	10

Ce-UiO-66-Cl	2.18	n/a	n/a	Calc.	10
Ce-UiO-66-Br	2.00	n/a	n/a	Calc.	10
Ce-UiO-66-I	1.53	n/a	n/a	Calc.	10
Ce-UiO-66-OH	1.41	n/a	n/a	Calc.	10
Ce-UiO-66-SH	0.95	n/a	n/a	Calc.	10
Ce-UiO-66-COOH	1.78	n/a	n/a	Calc.	10
Ce-UiO-66-CH_3	2.36	n/a	n/a	Calc.	10
Ce-UiO-66-CF_3	2.68	n/a	n/a	Calc.	10
Ce-UiO-66-SO_3H	2.20	n/a	n/a	Calc.	10
SUM-6	**1.55**	**n/a**	**n/a**	**Calc.**	**This work**
SUM-7	**1.69**	**n/a**	**n/a**	**Calc.**	**This work**
SUM-6	**1.42**	**8.4**	**2**	**Exp.**	**This work**
SUM-7	**1.79**	**46.4**	**2**	**Exp.**	**This work**

4.2 Mott-Schottky experiments
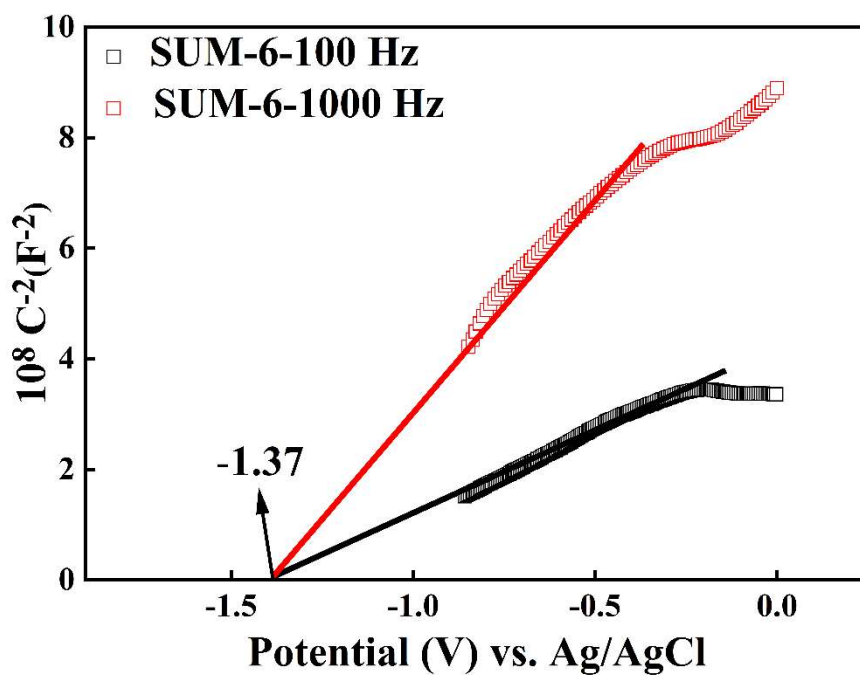
Figure S15. Mott-Schottky curves of SUM-6 at 100 Hz (black) and 1000 Hz (red).
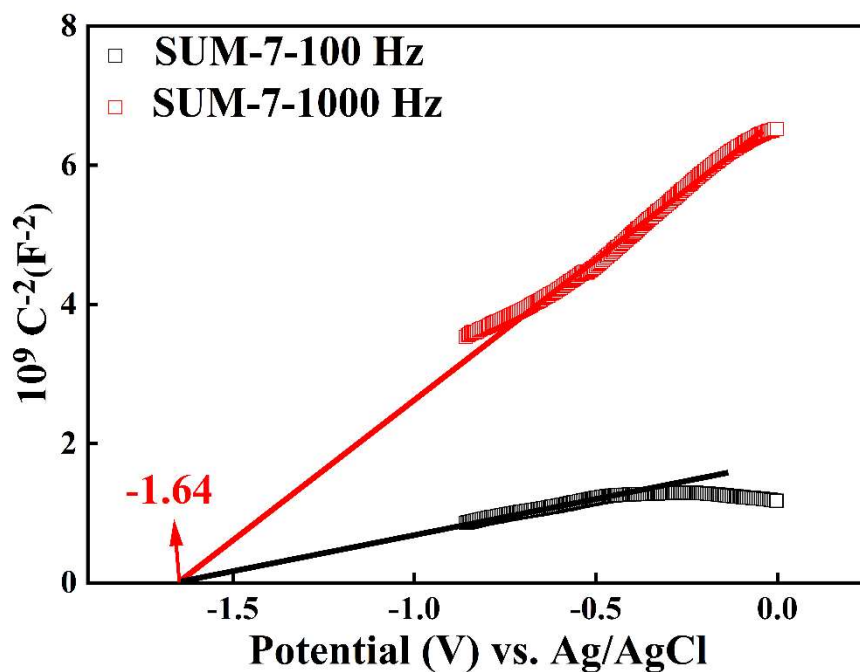

Figure S16. Mott-Schottky curves of SUM-7 at 100 Hz (black) and 1000 Hz (red).

The flat band potentials for SUM-6 and SUM-7 were determined based on the following Mott−Schottky equation using the data in the linear range:

$$\frac{1}{C^2} = \frac{2}{N_D e \varepsilon_0 \varepsilon}(E - E_{FB} - \frac{kT}{e})$$

Where C is the space charge capacitance in the semiconductor, N_D is the density of the charge carrier, e is the element charge, ε_0 is the permittivity of vacuum, ε is the relative permittivity of the semiconductor, E is the external potential, E_{FB} is the flat band potential, T is the temperature, k is the Boltzmann constant.

Carrier density N_D is calculated using the following equation based on Figures S15-S16 and Figure 2d of the main text:

$$N_D = \frac{2}{e \varepsilon_0 \varepsilon}(\frac{dE}{d(\frac{1}{C^2})})$$

Where $e = 1.6 \times 10^{-19}$ C, $\varepsilon_0 = 8.86 \times 10^{-12}$ F/m, and $\varepsilon = 48$.[11]

For SUM-6, $N_D = 8.86 \times 10^{19}$ cm^{-3}, SUM-7, $N_D = 1.30 \times 10^{19}$ cm^{-3}.

4.3 Photoluminescence

The fluorescence lifetimes of SUM-6 and SUM-7 were determined using the following equation based on a bi-exponential fit of the PL decay plots (Figures 3b and 3c of the main text).

$$R(t) = B_1 e^{(-t/\tau_1)} + B_2 e^{(-t/\tau_2)}$$

Table S4. Parameters of the bi-exponential fit of the PL decay plots

Name	τ_1 (ns)	Std. dev. (ns)	τ_2 (ns)	Std. dev. (ns)	X^2
SUM-6	0.5630	0.01492	5.3687	0.23607	1.197
SUM-7	1.9366	0.24962	18.7641	1.74820	1.067

4.4 Photocurrent measurements

Photocurrents were measured for SUM-6 and SUM-7 under illumination of a broad wavelength range (300–600 nm). However, for wavelengths > 430 nm, the photocurrents were small, therefore excluded from the plots shown below.
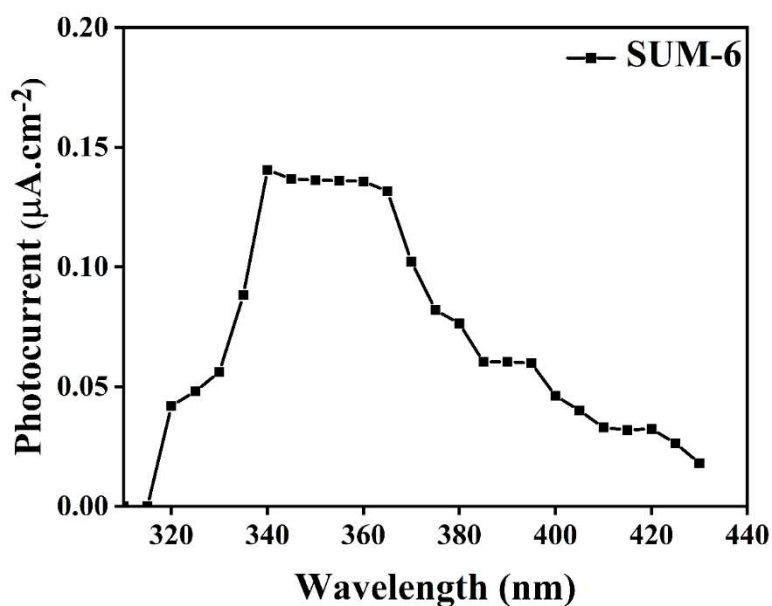
Figure S17. Photocurrent of SUM-6 under broad range irradiation.
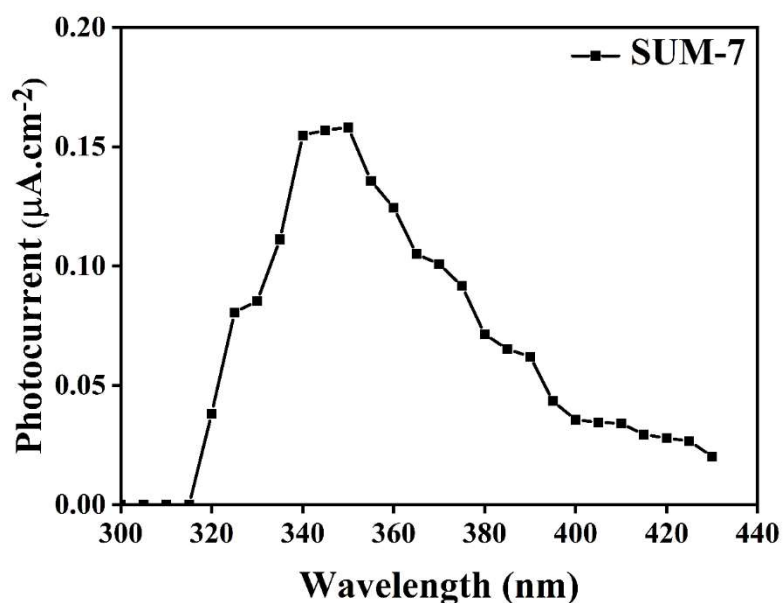
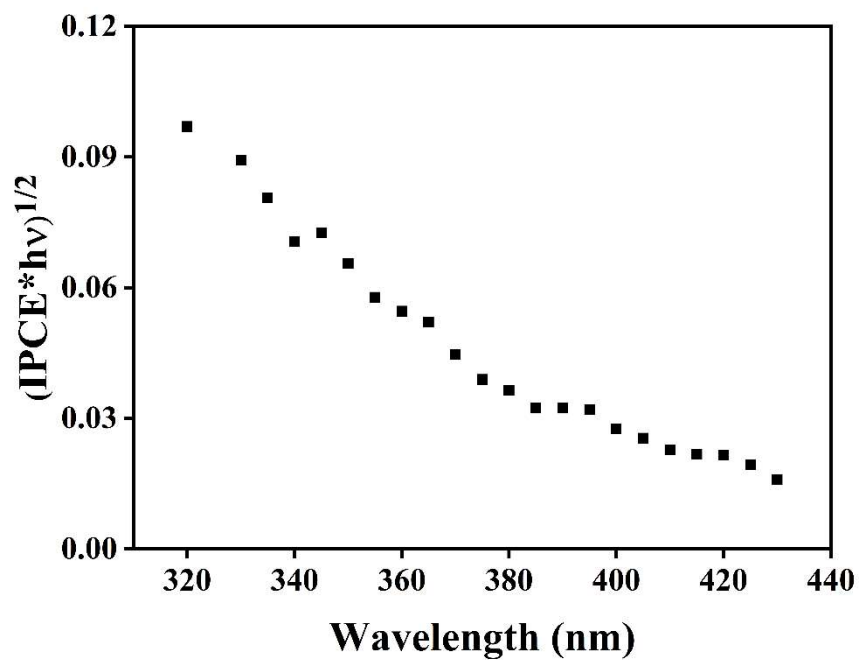**Figure S18.** Photocurrent of SUM-7 under broad range irradiation.
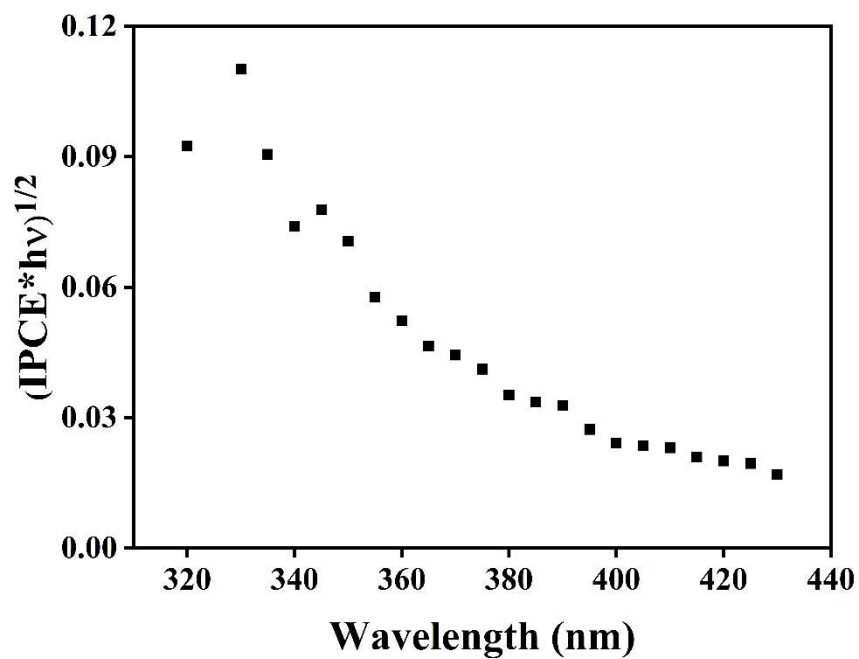
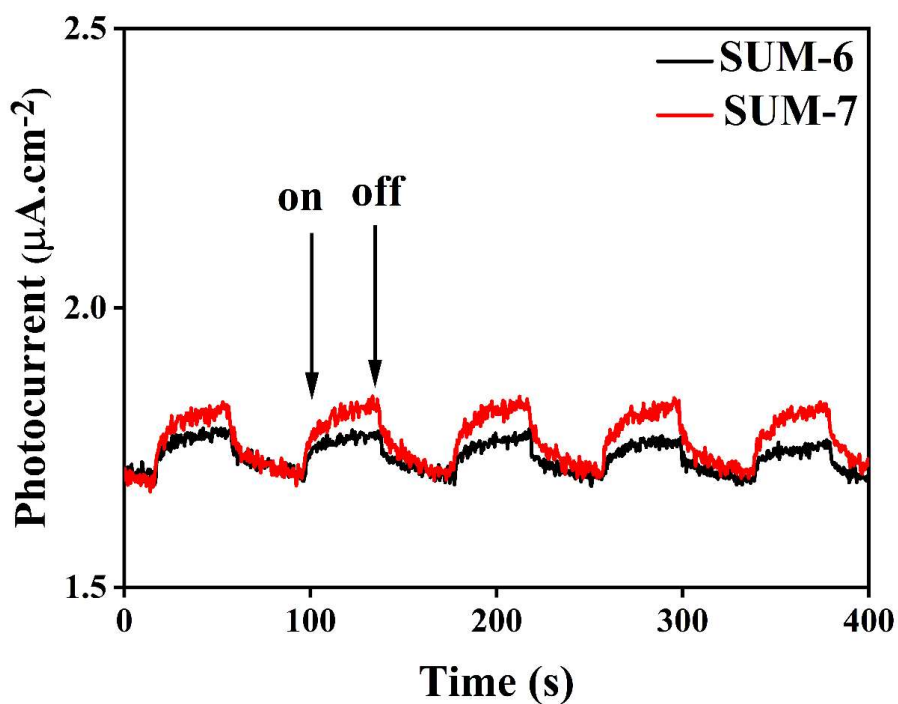**Figure S19.** IPCE plot of SUM-6.

Figure S20. IPCE plot of SUM-7.

Figure S21. Photocurrent transient for SUM-6 (black) and SUM-7 (red) with alternating light (410 nm) and dark cycles and a 1 V bias voltage.
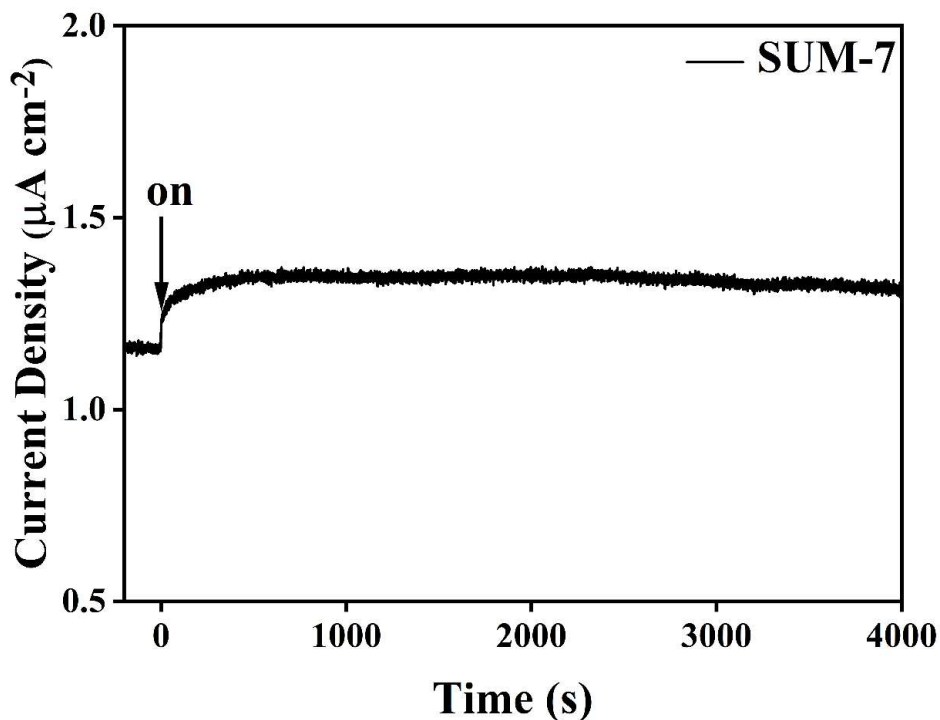

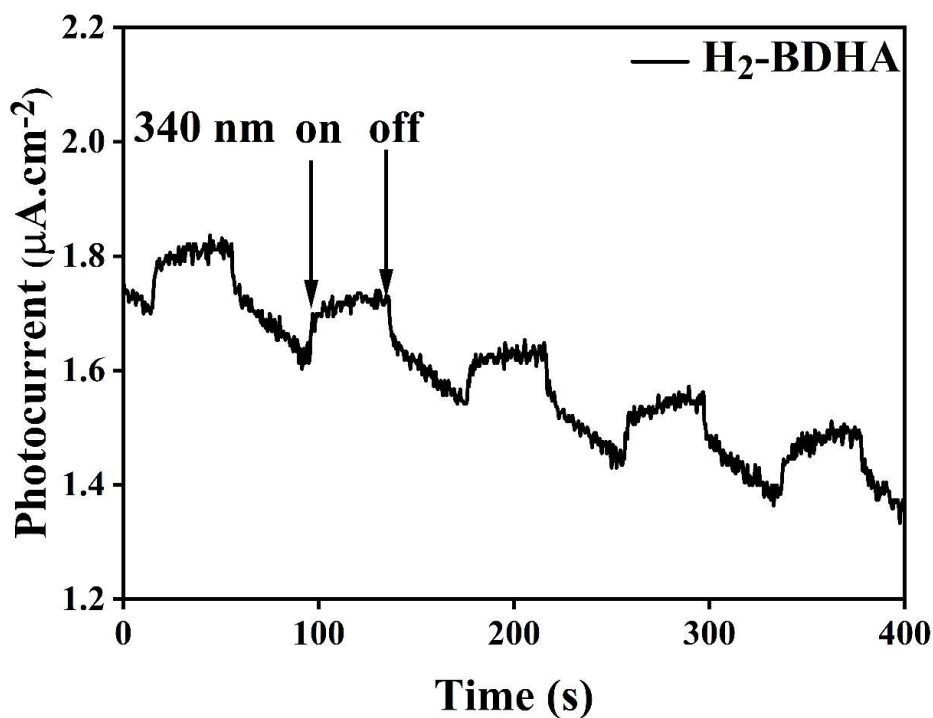**Figure S22.** Photocurrent stability over a period of 4000 s of SUM-7 when irradiated at 410 nm.

Figure S23. Photocurrent transient for H$_2$-BDHA with alternating light (340 nm) and dark cycles and a 1 V bias voltage.
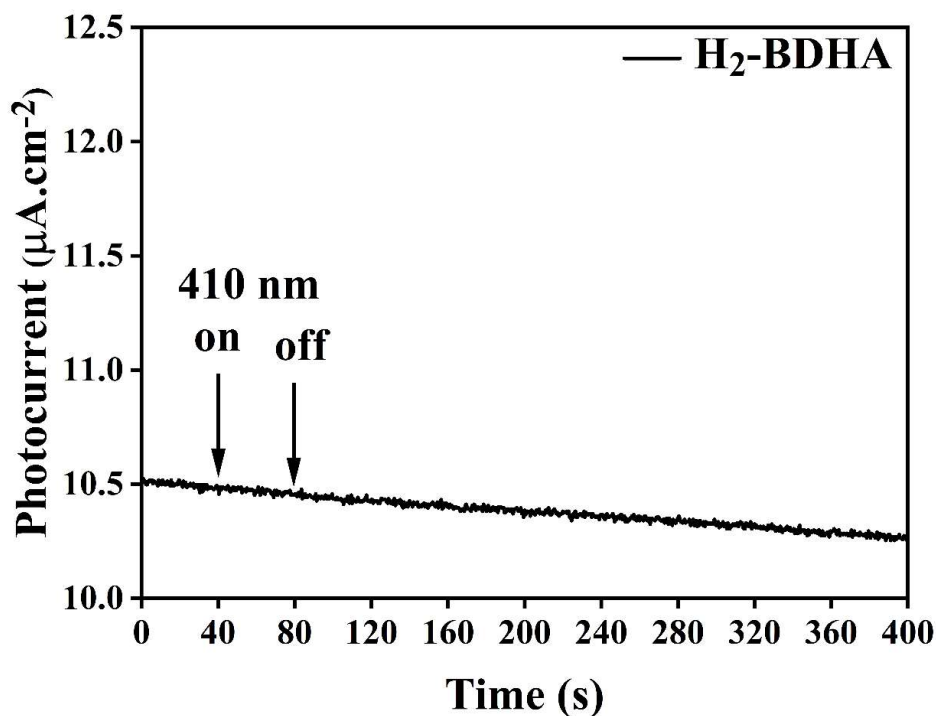

Figure S24. Chronoamperometric plots for H$_2$-BDHA with alternating light (410 nm) and dark cycles and a 1 V bias voltage.

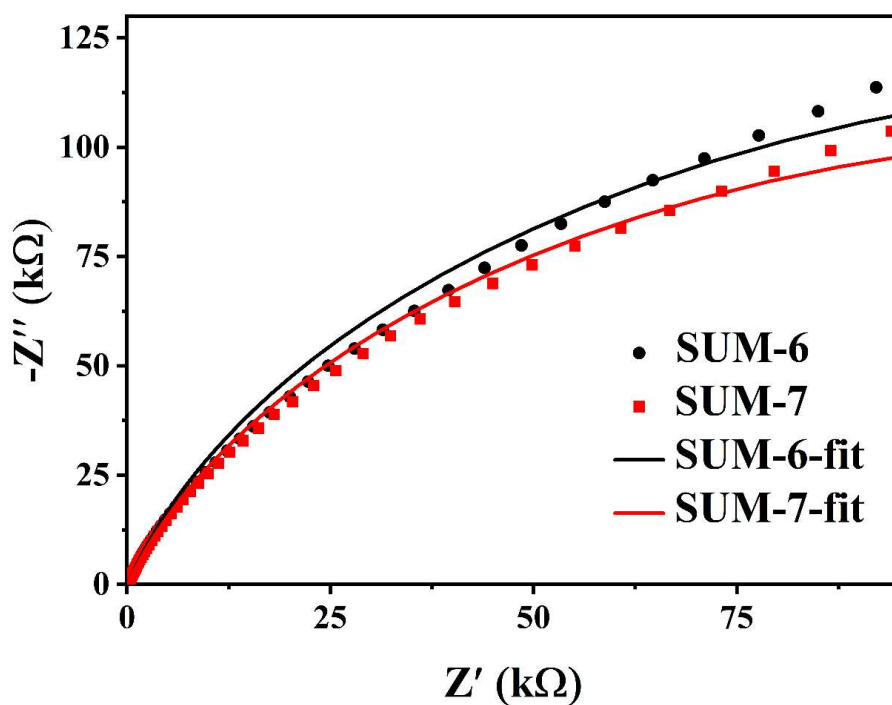4.5 Electrochemical Impedance Spectroscopy

Figure S25. Electrochemical impedance spectra of SUM-6 (black) and SUM-7 (red) and their corresponding fitted curves.
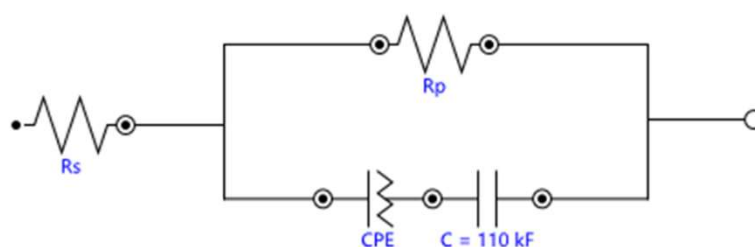

Figure S26. Equivalent circuit for the electrochemical impedance spectra.

Table S5. Fitting parameters of the equivalent circuit shown in Figure S26

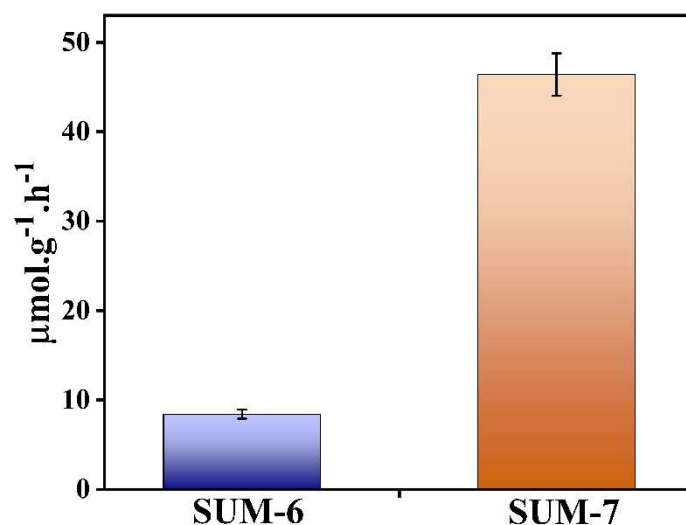| Name	Rp (kΩ)	Rs (Ω)	X^2
SUM-6	294	62	7.18
SUM-7	266	60.9	7.18

4.6 Photocatalytic H$_2$ generation

Figure S27. H$_2$ generation rates of SUM-6 and SUM-7.

SEM was used to monitor the morphology of MOF samples, before and after photocatalytic H$_2$ generation. In Figures 28 and S29, it was observed that the MOF crystals showed surficial corrosion and fragmentation that could be due to: (i) photocatalytic reaction; (ii) solvent evacuation during microscopic imaging.
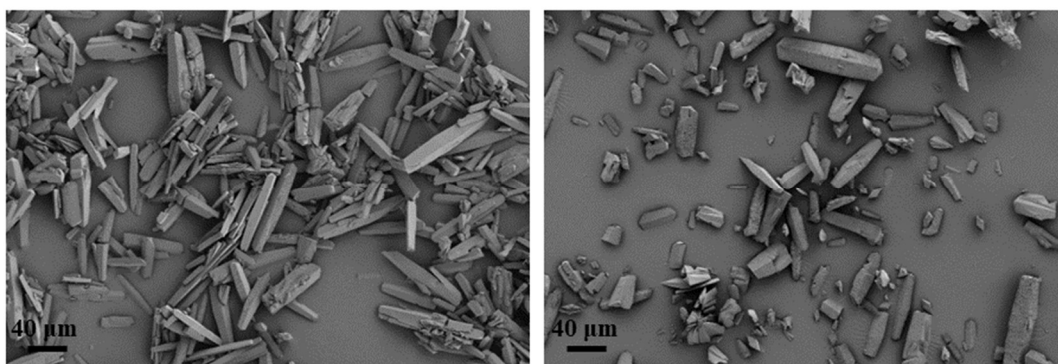

Figure S28. SEM images of as-synthesized SUM-6 (left) and sample after photocatalytic H$_2$ generation (right).
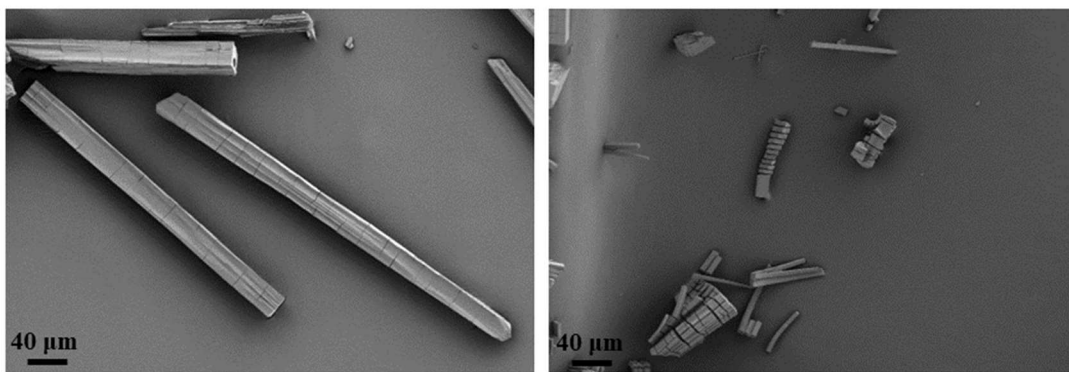
Figure S29. SEM images of as-synthesized SUM-7 (left) and sample after photocatalytic H_2 generation (right).

5. References

1. Sheldrick, G. M. A short history of SHELX. *Acta Crystallogr. A* **2008**, *64* (Pt 1), 112–122.

2. Sheldrick, G. M. Crystal structure refinement with SHELXL. *Acta Crystallogr. C* **2015**, *71* (Pt 1), 3–8.

3. Dolomanov, O. V.; Bourhis, L. J.; Gildea, R. J.; Howard, J. A. K.; Puschmann, H. OLEX2: a complete structure solution, refinement and analysis program. *J. Appl. Crystallogr.* **2009**, *42* (2), 339–341.

4. Lai, Q.; Chu, Z. Q.; Xiao, X.; Dai, D.; Song, T.; Luo, T. Y.; Tang, W.; Feng, X.; Zhang, Z.; Li, T.; Xiao, H.; Su, J.; Liu, C. Two-dimensional Zr/Hf-hydroxamate metal–organic frameworks. *Chem. Commun.* **2022**, *58* (22), 3601–3604.

5. Lerma-Berlanga, B.; Castells-Gil, J.; Ganivet, C. R.; Almora-Barrios, N.; González-Platas, J.; Fabelo, O.; Padial, N. M.; Martí-Gastaldo, C. Permanent Porosity in Hydroxamate Titanium−Organic Polyhedra. *J. Am. Chem. Soc.* **2021**, *143* (50), 21195–21199.

6. An, Y.; Liu, Y.; Bian, H.; Wang, Z.; Wang, P.; Zheng, Z.; Dai, Y.; Whangbo, M.-H.; Huang, B. Improving the photocatalytic hydrogen evolution of UiO-67 by incorporating Ce^{4+}-coordinated bipyridinedicarboxylate ligands. *Sci. Bull.* **2019**, *64* (20), 1502–1509.

7. Hu, Z.; Wang, Y.; Zhao, D. The chemistry and applications of hafnium and cerium(IV) metal–organic frameworks. *Chem. Soc. Rev.* **2021**, *50* (7), 4629–4683.

8. Melillo, A.; Cabrero-Antonino, M.; Navalón, S.; Álvaro, M.; Ferrer, B.; García, H. Enhancing visible-light photocatalytic activity for overall water splitting in UiO-66 by controlling metal node composition. *Appl. Catal., B* **2020**, *278*, 119345.

9. Gong, Y.-N.; Mei, J.-H.; Liu, J.-W.; Huang, H.-H.; Zhang, J.-H.; Li, X.; Zhong, D.-C.; Lu, T.-B. Manipulating metal oxidation state over ultrastable metal-organic frameworks for boosting photocatalysis. *Appl. Catal., B* **2021**, *292*, 120156.

10. Wu, X. P.; Gagliardi, L.; Truhlar, D. G. Cerium Metal−Organic Framework for

Photocatalysis. *J. Am. Chem. Soc.* **2018**, *140* (25), 7904–7912.

11. Chen, T. F.; Wang, L. Y.; Wang, Y. F.; Gao, H.; He, J.; Wang, G.; Meng, X. F.; Wu, Y. S.; Deng, Y. H.; Wan, C. Q. Facile Strategy for Efficient Charge Separation and High Photoactivity of Mixed-Linker MOFs. *ACS Appl. Mater. Interfaces* **2021**, *13* (17), 20897–20905.